ELSEVIER

Journal of Fluids and Structures 20 (2005) 993–1006

JOURNAL OF FLUIDS AND STRUCTURES

www.elsevier.com/locate/jfs

Nonlinear aeroelastic flutter phenomena of a flexible disk rotating in an unbounded fluid

A. Jana, A. Raman*

School of Mechanical Engineering, Purdue University, West Lafayette, IN 47907-2088, USA

Received 29 September 2004; accepted 16 May 2005

Abstract

Aeroelastic flutter in rotating disks is of interest in a number of applications including data storage systems, circular saws and microturbines. This paper presents new experimental results on the nonlinear aeroelastic flutter phenomena of a flexible disk rotating in an unbounded fluid. The experiments are performed on thin steel and paper disks over a wide range of rotation speeds in the post-flutter region with very fine, computer-controlled increments of the rotation speed. The existence of a primary instability of a reflected travelling wave of the disk, followed by a secondary instability, is confirmed. However, at speeds exceeding that at which the secondary bifurcation occurs, complicated, hitherto unrecorded nonlinear response is observed, including several solution branches and bifurcation points, frequency lock-ins over certain rotation speed ranges, presence of higher harmonics of the unstable wave and large frequency and amplitude hysterisis, as the disk speed is ramped up and down across these bifurcations. It is shown that a nonlinear von Kármán plate model for the disk, coupled with a linear aerodynamic load having the form of a rotating damping pressure, is capable of capturing the primary instability branch. However, such a model is inadequate in capturing the secondary bifurcation and the complicated nonlinear response that follows.

Keywords: Vibration; Spinning disc; Fluid–structure interaction

1. Introduction

Aeroelastic flutter poses serious challenges in the design of high-speed disks rotating in air. Practical applications include circular saws, CD and DVD drives and microscale turbine rotors. In such applications, the trend is to design disks with reduced thicknesses and higher rotation speeds, making these disks more and more prone to experience aerodynamically induced self-excited vibrations during operation. A thorough understanding of aeroelastic flutter is hence required to design these next-generation rotating disk systems.

Some early experiments on aeroelastic flutter of rotating disks were performed by Stakhiev (1972) and Bouchard and Talke (1986). More detailed experimental and theoretical investigations have been attempted recently. One body of research, relevant for floppy and zip disks, concerns the flutter of rotating disks supported on very thin air films (Hosaka and Crandall, 1992; Huang and Mote, 1995; Renshaw, 1998; Naganathan et al., 2002). Because of the low Reynolds number of the fluid film, these analyses use the incompressible Reynolds' equation of classical hydrodynamic

*Corresponding author. Tel.: +1 765 494 5733; fax: +1 765 494 0539.
E-mail address: raman@ecn.purdue.edu (A. Raman).

0889-9746/$ - see front matter © 2005 Published by Elsevier Ltd.
doi:10.1016/j.jfluidstructs.2005.05.010

lubrication theory to couple the film pressure to the disk vibration. However, such models are inapplicable for a disk rotating in an unbounded fluid medium or inside a large fluid-filled enclosure.

D'Angelo and Mote (1993) first published extensive experimental results on the flutter of a thin steel disk rotating in open air as well as in a large enclosure. They measured the flutter speeds, and photographed the fluttering travelling waves using Moiré photography, providing direct evidence that the flutter is due to the instability of a single reflected travelling wave (RTW). At pre-flutter speeds, they observed the well-known frequency-speed behavior characteristic of a rotating disk: a backward travelling wave (BTW) frequency vanished at the disk critical speed, and the BTW became a RTW with increasing frequency at super-critical speeds. The vibration amplitude remained small at pre-flutter speeds. However, beyond the flutter speed, the amplitude of the unstable RTW grew rapidly. A frequency lock-on of the unstable RTW also occurred. Lee et al. (2003) reported the same post-flutter phenomena for two optical disks—a CD and an ASMO disk.

Raman et al. (2002) repeated the experiment of D'Angelo and Mote (1993) in an enclosure over a small speed range about the flutter speed with smaller increments in the rotation speed. They observed that two separate instabilities occur in rapid succession as the disk crossed the flutter speed. A primary instability occurred at the flutter speed, triggering a rapid growth in the amplitude of the unstable RTW as the rotation speed increased beyond the flutter speed. The frequency of the unstable RTW continued to increase with speed. A little into the post-flutter region, a secondary instability occurred, causing a sudden, large increase in the RTW amplitude and a simultaneous, sudden decrease in its frequency. Beyond the secondary instability, the RTW amplitude continued to increase, but its frequency remained locked on. With decreasing speed, the above chain of events was reversed, but significant hysterisis in the response was observed.

Several theoretical analyses on the prediction of the aeroelastic flutter speed of rotating disks based on linear disk and fluid models have been published. Yasuda et al. (1992) proposed an ad hoc distributed rotating damping representation for the aerodynamic load on the rotating disk. Hansen et al. (2001) and Kim et al. (2000) presented an experimental parameter-extraction procedure based on the rotating damping model to predict of the flutter speeds of an unenclosed and an enclosed disk, respectively. Renshaw et al. (1994) attempted the theoretical prediction of flutter speeds of unenclosed and enclosed disks with zero material damping, using compressible potential flow aerodynamics. Jana and Raman (2004) suggested some modifications of the work of Renshaw et al. (1994), and extended it to materially damped disks rotating in an unbounded fluid. Kim and Renshaw (2002) proposed an alternative theory based on discontinuities in the fluid motion arising from boundary layers near the disk periphery to predict the flutter speed of an unenclosed disk.

A few nonlinear analyses of the response of a disk rotating in an unbounded fluid have also been published. Nowinski (1984) studied the nonlinear free vibrations of a circular membrane rotating in a viscous fluid. The only viscous effect he included was the circumferential shear traction on the rotating disk, which contributes to the in-plane membrane stresses. No aeroelastic flutter instability is predicted in this paper. Hansen (1999) considered a nonlinear von Kármán plate model for the disk coupled with a linear aerodynamic load having the form of a rotating damping pressure. He analyzed this model using the method of multiple scales and obtained an analytical expression for amplitude and frequency of the primary instability branch. His predicted growth in amplitude of the primary instability branch matches qualitatively the experimental results of D'Angelo and Mote (1993).

The main contribution of this paper is to present new experimental observations on the post-flutter nonlinear aeroelastic response of a flexible disk rotating in an unbounded fluid. In addition, it is also demonstrated that the nonlinear aeroelastic model investigated by Hansen (1999) provides not only qualitative, but good quantitative match with our experimentally measured amplitudes and frequencies for the primary instability branch. Accordingly, the paper is organized into two main sections. Section 2 describes in detail the experimental set-up, experimental procedure and results. The nonlinear post-flutter responses of thin steel disks as well as paper disks are presented. Section 3 begins with an outline of the nonlinear model of Hansen (1999). The amplitudes and frequencies of the primary instability branch are then computed in AUTO 97 (Doedel et al., 1998) using this nonlinear model and are compared with our experimental measurements. It is shown that the inclusion of plate geometric nonlinearities predicts reasonably accurately the growth in amplitude following the onset of flutter. Finally, the conclusions are summarized in Section 4.

2. Experiments

2.1. Experimental set-up

A schematic of the experimental set-up is shown in Fig. 1. The experiments are performed on a T1000 spinstand, custom-built by TTI Inc (www.tti-us.com), a manufacturer of equipments for the testing of hard disk drives. The

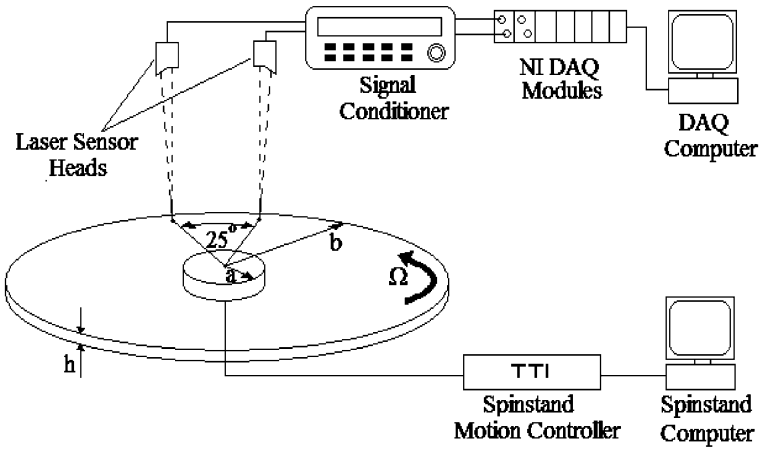

Fig. 1. The experimental set-up.

spinstand is capable of rotating a disk at up to a maximum speed of 30 000 r.p.m., with accurate computer control of the rotation speed. Various user-defined speed profiles can be realized. The maximum recommended angular acceleration is 2500 r.p.m./s. The spindle on which the disk is mounted is extremely stiff, with lowest natural frequency approximately 800 Hz. The clamping diameter for the disk is 27.94 mm. A special clamping head achieves an almost uniform clamping pressure everywhere along the edge of the clamp. The transverse displacement of the disk is measured using a Microtrak 7000 laser displacement sensor system manufactured by MTI Instruments. Two MT600 diffuse-type laser sensor heads are used to measure the disk transverse displacement at two different locations near the periphery of the disk that are separated angularly by 25°. The two-sensor data facilitate the subsequent modal identification using the cross-power spectrum of the two data channels (Ahn and Mote, 1998). Time histories of the vibration signal are acquired using the SCC-AI data acquisition modules and the LabView software from National Instruments. Frequency analysis of the time histories are performed in MATLAB.

2.2. Post-flutter experiments on thin steel disks

2.2.1. Experimental procedure

The experiments were repeated several times on a collection of steel disks having the same outer diameter but different thicknesses in the range of 0.1016–0.3048 mm. The data are quite repeatable in each case. The disks are machined from cold-rolled steel shim stock. Each disk is slightly warped when stationary, but centrifugal stresses flatten the disk as it starts rotating. During a particular run of the experiment, the disk rotation speed is first increased from 1000 to 11 000 r.p.m. and then decreased from 11 000 to 1000 r.p.m. in steps of 50 r.p.m. Each 50 r.p.m. step is generated at a uniform acceleration of 100 r.p.m./s. At each rotation speed, 150 s long time histories of the disk transverse vibration are captured at a sampling rate of 1 kHz/channel. The power spectrums of both channels and the cross-spectrum between the two channels of data are computed in MATLAB for each pair of time histories using the Welch periodogram algorithm. For each of these computations, the specific time history is segmented into 39 overlapping sections with 50% overlap using the Hanning window, and each segment of time history is zero-padded to four times the smallest power of 2 that is greater than the segment length. Each (m, n) forward, backward or reflected travelling wave mode (FTW, BTW or RTW) of the rotating disk corresponds to a peak in the power spectrum. Here m is the nodal circle number and n is the nodal diameter number of the particular wave. The above peaks are matched with their corresponding nodal diameter numbers by utilizing the cross-spectrum between the two channels of data (Ahn and Mote, 1998). Finally, at each rotation speed, the frequencies and amplitudes of the travelling wave modes are extracted.

2.2.2. Experimental results

In this section, a typical set of experimental post-flutter response data, for a specific steel disk whose properties are listed in Table 1, is presented in detail. The results are qualitatively similar for all steel disks tested. Figs. 2 and 3 are the waterfall plots of the measured power spectrums of transverse disk vibration, during rotation speed sweeps up and

Table 1
Properties of the steel disk used for the experimental data presented in Section 2.2.2

Property	Value
Outer diameter (mm)	190.5
Inner diameter (mm)	27.94
Thickness (mm)	0.254
Density (kg/m^3)	7700
Young's modulus (GPa)	207
Poisson's ratio	0.3

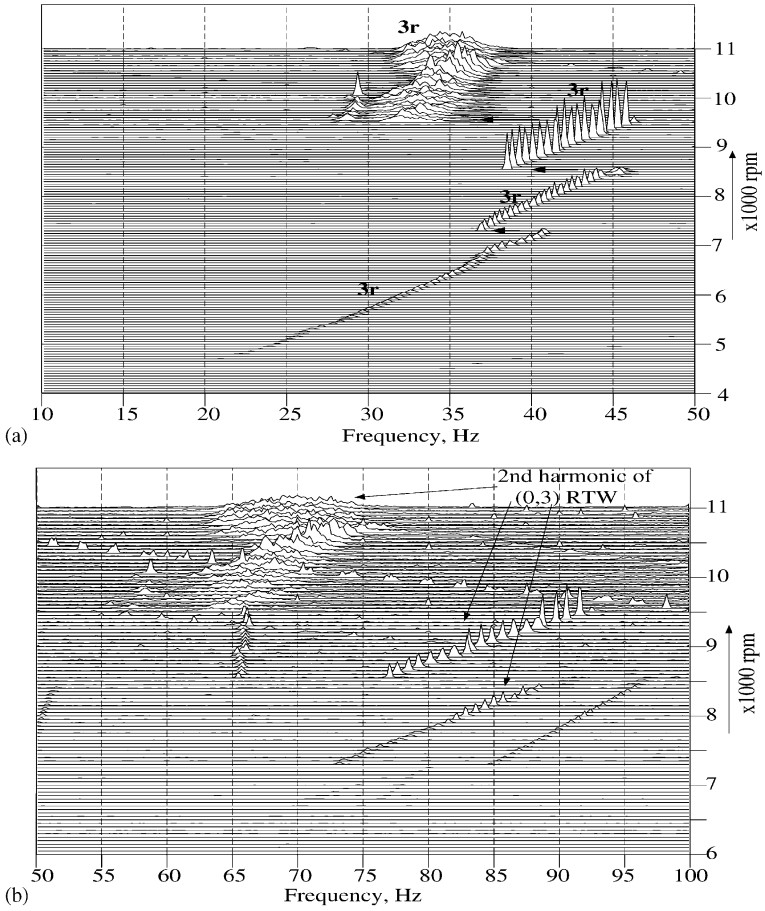

Fig. 2. Waterfall plots of the power spectral densities of the transverse vibration of the 0.01 in thick steel disk during rotation speed sweep up: (a) the fundamental (0, 3) RTW (denoted by 3r) and (b) the second harmonic of the (0, 3) RTW. The power spectral density scale for figure (b) has been magnified 10 times.

down, respectively. Figs. 4 and 5 show the variations with the rotation speed of the frequency and the amplitude of the (0, 3) and (0, 4) RTW, respectively.

The experiments indicate that the primary flutter mode is the (0, 3) RTW, and the corresponding flutter speed is approximately 4425 r.p.m. The flutter speed is determined by noting in Fig. 4 that the amplitude of the (0, 3) RTW at 4450 r.p.m. suddenly nearly doubles compared to its maximum amplitude for rotation speeds $\Omega \leqslant 4400$ r.p.m. (see also Fig. 8). As the rotation speed is increased beyond 4450 r.p.m., the (0, 3) RTW amplitude grows rapidly. Hence the

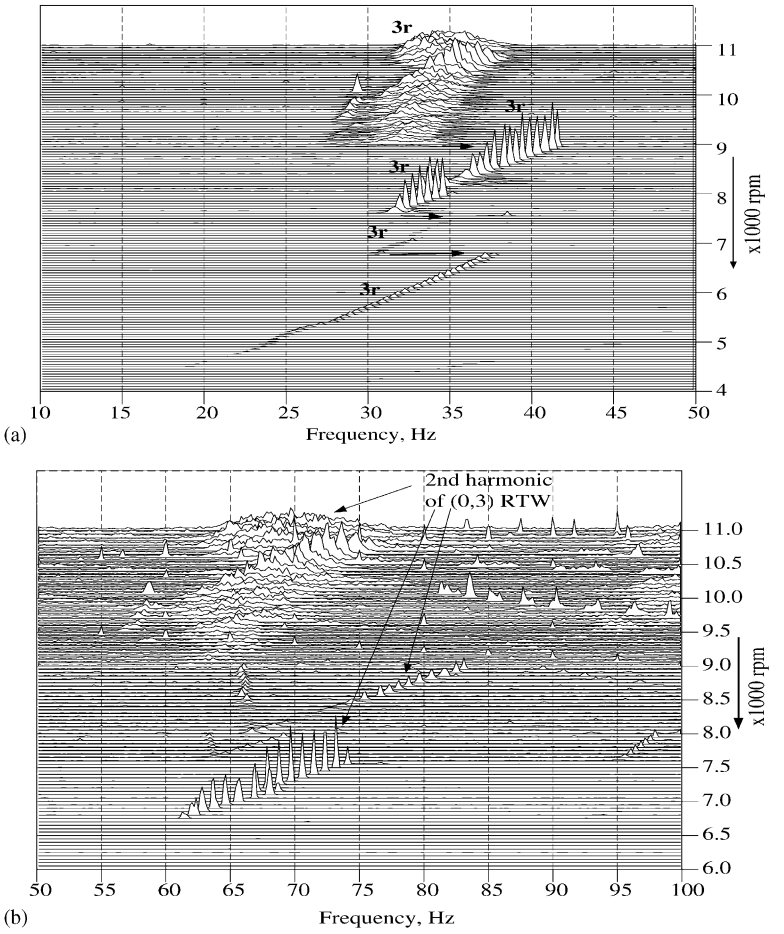

Fig. 3. Waterfall plots of the power spectral densities of the transverse vibration of the 0.01 in thick steel disk during rotation speed sweep down: (a) the fundamental (0, 3) RTW (denoted by 3r) and (b) the second harmonic of the (0, 3) RTW. The power spectral density scale for figure (b) has been magnified 10 times.

flutter instability of the (0, 3) RTW is said to occur between 4400 and 4450 r.p.m. The average of 4425 r.p.m. is chosen as the flutter speed, that is, $\Omega_f \approx 4425$ r.p.m. As the disk speed is increased beyond the flutter speed, the frequency and amplitude of the (0, 3) RTW solution continue to increase along branch I. Raman et al. (2002) refer to the flutter instability as the primary instability and the solution branch I as the primary instability branch.

Fig. 4 reveals the existence of multiple solution branches and bifurcation points for the primary flutter mode, the (0, 3) RTW, in the post-flutter region. All bifurcations occurring in the post-flutter region can be termed secondary instabilities. The first secondary instability occurs at point A, when the solution jumps from branch I to II with a sudden decrease in frequency, but no significant jump in amplitude. As the rotation speed is ramped up further, additional bifurcations occur at point B, when the solution jumps from branch II to III with a sudden decrease in frequency and a sudden large increase in amplitude, and then at point C, when the solution jumps from branch III to branch IV with a sudden decrease in both the frequency and the amplitude. Beyond point C, the solution appears to remain on branch IV. However, a spike in both the amplitude and the frequency is observed around 10 500 r.p.m. As the rotation speed is decreased from 11 000 r.p.m., the first bifurcation occurs at point D, when the solution jumps from branch IV to III with a sudden increase in both the frequency and the amplitude. As the speed is lowered further, the solution jumps to branch V at E with a small increase in frequency but no discernible change in amplitude. However just prior to this bifurcation, there is a sudden inexplicable dip in amplitude at around 8200 r.p.m. Subsequently, at point F the solution jumps from the high amplitude branch V to the very low amplitude branch VI accompanied again by a small upward jump in frequency. Finally, at

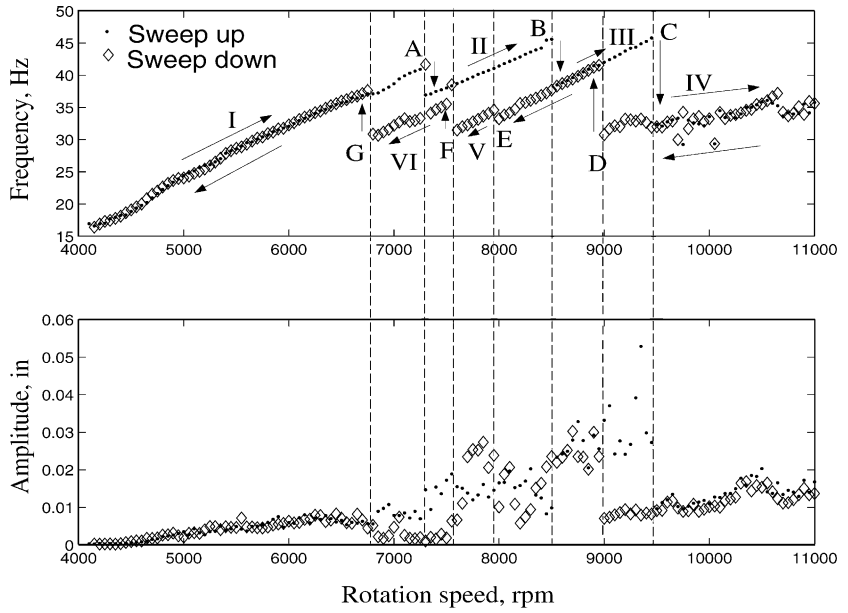

Fig. 4. Variation of the frequency and amplitude of the (0, 3) RTW of the 0.01 in thick steel disk.

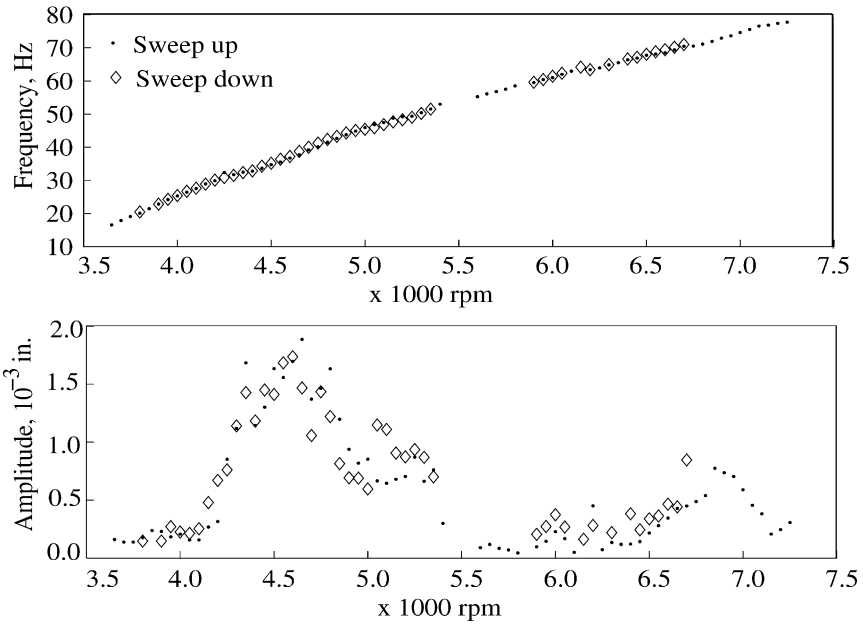

Fig. 5. Variation of the frequency and amplitude of the (0, 4) RTW of the 0.01 in thick steel disk.

point G it jumps back to the primary instability branch I. This last bifurcation is accompanied by an upward jump in both the frequency and the amplitude. On reducing the speed further, the (0,3) RTW retraces back the primary instability branch I. Note that the response for the (0, 3) RTW exhibits considerable frequency and amplitude hysterisis. Certain solution branches are traversed only on the rotation speed sweep up, while certain others are traversed only on the sweep down. The number and location of the jumps during the sweep up are also different from those during the sweep down.

The different solution branches that coexist in the post-flutter region have different characteristics. Excepting branch IV, along all other solution branches the frequency increases as the rotation speed increases. On branch IV, however, the frequency of the (0, 3) RTW is approximately locked in. Additionally, branch IV is characterized by distinctly wider peaks (see Figs. 2 and 3). Branches III and V are characterized by large amplitudes, while along branch VI the amplitude is surprisingly low. The amplitude also remains approximately constant along this branch.

A careful inspection of the waterfall plot in the frequency range of 50–100 Hz (Figs. 2(b) and 3(b)) reveals the existence of the second harmonic of the large amplitude fundamental (0, 3) RTW at speeds greater than approximately 7000 r.p.m. The amplitude of the second harmonic is approximately 20% of the amplitude of the fundamental (0, 3) RTW. Thus the circumferential harmonic spatial form of the main fluttering wave is significantly distorted at high rotation speeds in the post-flutter region.

Some interaction may exist between modes possessing different nodal diameter numbers. For example, just prior to the flutter instability for the (0, 3) RTW, a growth in the amplitude of the (0, 4) RTW is observed, beginning from around 4100 r.p.m. After the flutter instability of the (0, 3) RTW has set in, the amplitude of the (0, 4) RTW collapses gradually. Over the speed range from 5300 to 6500 r.p.m., the (0, 4) RTW amplitude remains extremely small, often becoming indistinguishable from noise. The (0, 4) RTW amplitude exhibits a moderate growth again in the speed range from 6400 to 7000 r.p.m. At speeds greater than 7000 r.p.m., the (0, 4) RTW peak again becomes indistinguishable from noise. Note that the frequency of the (0, 4) RTW continuously increases in an almost linear fashion over the entire observable speed range. Furthermore, no significant frequency and amplitude hysterisis is associated with the response for this mode.

2.3. Post-flutter experiments on thin paper disks

2.3.1. Experimental procedure

Next, the experiments are repeated on paper disks that are media with much lower bending stiffness and much greater internal damping than steel. The experiments are performed several times on a set of paper disks cut out from 27.9×35.6 cm sheets of Smooth Bristol art paper manufactured by Canson Inc. (www.canson-us.com). All the paper disks possess nominally identical properties, which are listed in Table 2. In each run of the experiment, the rotation speed of the paper disk is increased from 3000 to 9000 r.p.m. and then decreased from 9000 to 3000 r.p.m. in steps of 50 r.p.m. Each 50 r.p.m. step is generated at a uniform acceleration of 100 r.p.m./s. The initially slightly warped disk is flattened by centrifugal stresses as it starts rotating. The vibration data is captured and analyzed in exactly the same way as for the steel disk.

2.3.2. Experimental results

Fig. 6 shows the waterfall plots of a typical set of vibration data for a paper disk during rotation-speed sweep up. The vibration data for rotation-speed sweep down is similar to that during sweep up, albeit with some frequency and amplitude hysterisis. The main flutter mode for the paper disk is also the (0, 3) RTW. Fig. 7 shows the variations of the frequency and the amplitude of the (0, 3) RTW with rotation speed in the post-flutter region. The post-flutter behavior of the paper disk also features multiple solution branches and bifurcation points and frequency and amplitude hysterisis. However, the number and nature of the solution branches and the number and location of the secondary bifurcations are quite different. The multiple solution branches and the jumps are not as distinct and conspicuous for the paper disk as for the steel one. Furthermore, as in the steel disk, the harmonic spatial form of the large amplitude fluttering wave in the circumferential direction becomes distorted at high rotation speeds. Both the second and the third harmonic of the main fluttering (0, 3) RTW can be detected for the paper disk.

Table 2
Nominal properties of the paper disks

Property	Value
Outer diameter (mm)	152.4
Inner diameter (mm)	27.94
Thickness (mm)	0.2921
Density (kg/m^3)	770

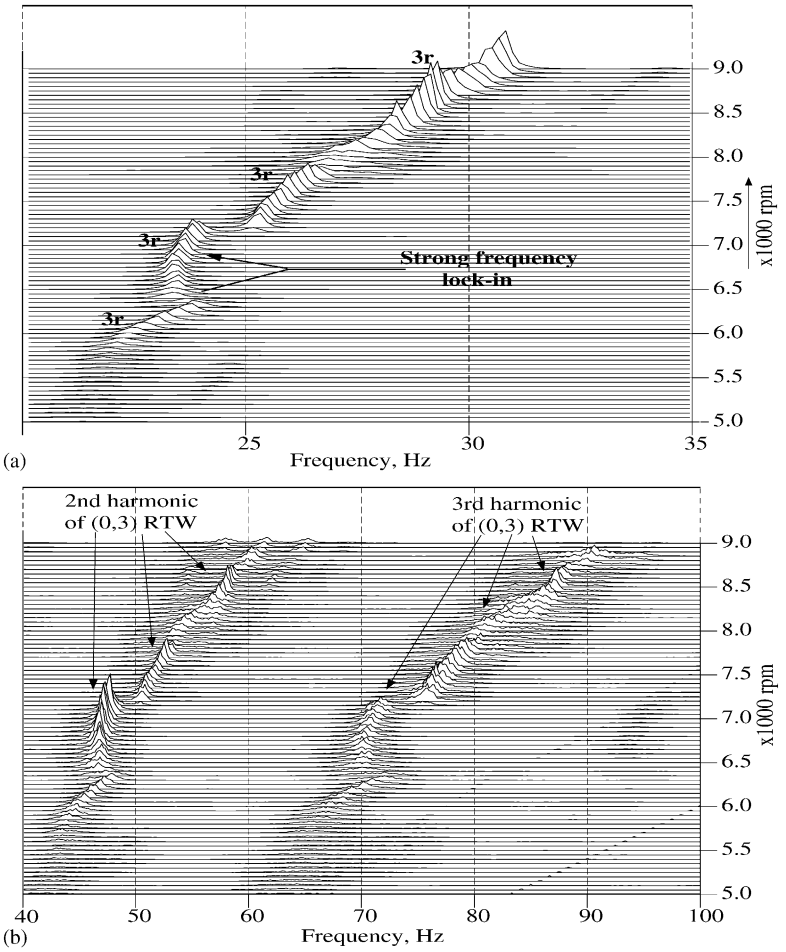

Fig. 6. Waterfall plots of the power spectral densities of the transverse vibration of the paper disk during rotation speed sweep up: (a) the fundamental (0, 3) RTW (denoted by 3r) and (b) the higher harmonics of the (0, 3) RTW. The power spectral density scale for figure (b) has been magnified 10 times.

Figs. 6 and 7 reveal interesting frequency lock-in behavior for the paper disk. Over the speed range of 4000–9000 r.p.m., the total variation in the frequency of the (0, 3) RTW is ~10 Hz. Thus it may be concluded that the frequency of the (0, 3) RTW is approximately locked in over the entire observed speed range in the post-flutter region. Further, it is observed that there exist pockets of rotation speeds over which the (0,3) RTW frequency is very strongly locked in. Outside these speed pockets, the frequency varies slowly with rotation speed. The strong frequency lock-ins are not observed in the case of the 0.01 in thick steel disk described earlier. However such lock-ins are present in the post-flutter responses of the thinner steel disks tested. Note that the pockets of strong frequency lock-in exist both during sweep up and down, but does not necessarily occur over the same rotation speed ranges.

2.4. Discussion of the experimental results

The following are the key post-flutter response features that are observed to exist for the entire spectrum of disks tested:

(i) existence of multiple solutions and bifurcation points beyond the primary flutter instability and transitions between branches accompanied by jumps in the frequency and amplitude;

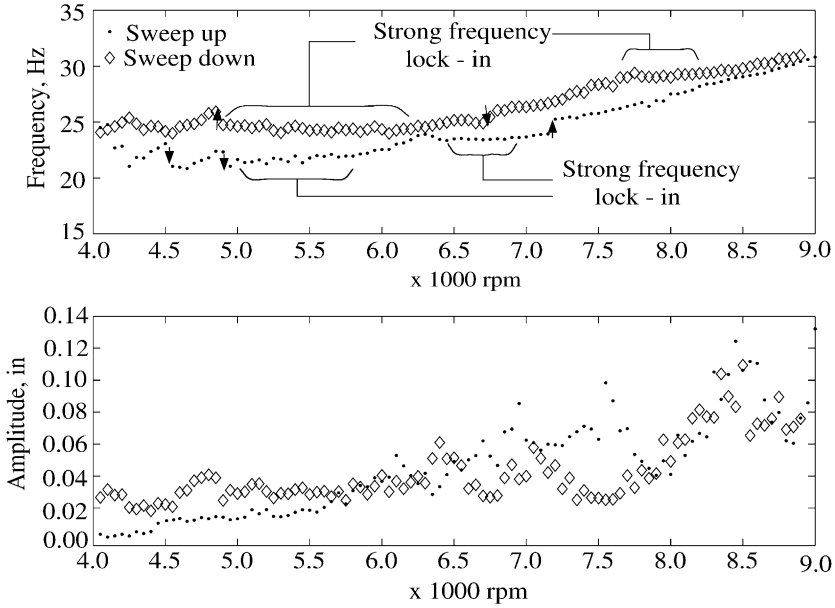

Fig. 7. Variation of the frequency and amplitude of the (0, 3) RTW of the paper disk.

(ii) harmonic distortion of the shape of the large amplitude fluttering wave in the circumferential direction;
(iii) frequency and amplitude hysterisis; and
(iv) approximate lock-in of the frequency of the unstable wave at high rotation speeds.

Strong frequency lock-ins over small pockets of rotation speed are also observed for paper as well as for ultra-thin steel disks. Such effects are nonexistent for thicker steel disks. Clearly, the rich post-flutter dynamics observed poses difficult modeling challenges. Note that, although the specific details of the post-flutter response vary amongst different disks, they are quite repeatable for a particular disk.

The current experimental observations are substantially more complicated than those previously reported (D'Angelo and Mote, 1993; Lee et al., 2003; Raman et al., 2002). The steel disks used in the current experiments have approximately half the diameter and 10–30% of the thickness of the steel disk used in the experiments of D'Angelo and Mote (1993) and Raman et al. (2002). The smaller thicknesses of the present disks imply much lower bending stiffnesses. The range of values of the Reynolds number,[1] over the observed post-flutter region of the present steel disks is $\mathrm{Re}_b \approx 2.5 \times 10^5$–$7 \times 10^5$. For the experiments of D'Angelo and Mote (1993), this range is $\mathrm{Re}_b \approx 6.5 \times 10^5$–$13 \times 10^5$. Clearly, the post-flutter responses presented in this work are for different regimes of system parameters such as the bending stiffness and Reynolds number, compared to previous work. Hence it is possible that the physics underlying the current experiments is different, producing a much more complicated post-flutter response.

3. Nonlinear analysis of the post-flutter dynamics

In this section, a nonlinear aeroelastic model is adopted to investigate the primary instability branch over a small range of rotation speeds around the onset of flutter. Hansen (1999) analyzed the same model using the method of multiple scales. In this paper, the analysis is performed using the continuation and bifurcation software AUTO97 (Doedel et al., 1998). Unlike perturbation techniques such as multiple scales, AUTO97 is not restricted to systems with weak nonlinearities.

[1]The Reynolds number calculations are based on $\mathrm{Re}_b = b^2\Omega/\nu$, where b is the outer disk radius and $\nu = 1.5 \times 10^{-5}\,\mathrm{m}^2/\mathrm{s}$ is the kinematic viscosity of air at 20 °C.

3.1. Governing PDEs and discretization

An annular disk of uniform thickness h, clamped at inner radius a and free at outer radius b, rotates about its axis in the counter-clockwise direction at a constant angular speed Ω, as shown in Fig. 1. The disk is thin, homogeneous, isotropic and linearly elastic, with mass density ρ_d, Young's modulus E and Poisson's ratio ν. Let $D = Eh^3/(12(1-\nu^2))$ be the bending stiffness of the disk and $F(r,\theta,t)$ be the transverse aerodynamic pressure differential on the disk. $(\mathbf{e_r}, \mathbf{e_\theta}, \mathbf{e_z})$ form the cylindrical basis for a ground-fixed reference frame, with its origin fixed at the intersection of the midplane of the disk and its axis, and $\mathbf{e_z}$ oriented along this axis. The disk is modeled as a von Kármán plate with rotation-speed-dependent membrane stresses. The nonlinear field equations governing the transverse displacement $w(r,\theta,t)$ of the midplane of the disk and the membrane stress function $\Phi_0(r,\theta,t)$ arising from nonlinear bending effects were first derived by Nowinski (1964). A brief derivation of the disk governing partial differential equations (PDEs) and their discretization can also be found in Nayfeh (2000). With the introduction of the following dimensionless quantities,

$$r' = \frac{r}{b}, \quad z' = \frac{z}{b}, \quad a' = \frac{a}{b}, \quad w' = \frac{bw}{h^2}, \quad t' = \frac{t}{b^2}\sqrt{\frac{D}{\rho_d h}},$$
$$\Omega' = \frac{\mathrm{d}\theta}{\mathrm{d}t'}, \quad \varepsilon = \frac{12(1-\nu^2)h^2}{b^2}, \quad \Phi' = \frac{b^2\Phi}{Eh^4}, \quad F' = \frac{Fb^5}{Dh^2}, \tag{1}$$

the governing nonlinear PDEs become

$$w_{,tt} + 2\Omega w_{,t\theta} + \Omega^2 w_{,\theta\theta} + \mathscr{C}_d\left[w_{,t} + \Omega w_{,\theta}\right] + L_\Omega^{r\theta}[w] = \varepsilon L_N[w,\Phi_0] + F,$$
$$\nabla^4\Phi_0 = -\tfrac{1}{2}L_N[w,w], \tag{2}$$

where $\mathscr{C}_d[\cdot]$ is a spatial operator modeling structural dissipation, $L_\Omega^{r\theta}[\cdot]$ is the linear stiffness operator consisting of the plate bending stiffness and the rotation-induced membrane stresses and $L_N[f,g]$ is the Mongé–Amperé bilinear form. Note that the primes have been dropped in Eq. (2) and the subsequent analysis.

It has been shown in prior work (Yasuda et al., 1992; Hansen et al., 2001) that for predicting the onset of the flutter instability, the aerodynamic pressure differential $F(r,\theta,t)$ can be represented as a rotating damping pressure that rotates in the same sense as the disk, albeit slower than it. Hence with respect to the ground-fixed frame, $F(r,\theta,t)$ can be represented by

$$\begin{aligned} F(r,\theta,t) &= -\mathscr{C}_f[w_{,t} + (\Omega - \Omega_d)w_{,\theta}] \\ &= -\frac{\Omega_d}{\Omega}\mathscr{C}_f[w_{,t}] + \left(1 - \frac{\Omega_d}{\Omega}\right)\mathscr{C}_f[w_{,t} + \Omega w_{,\theta}], \end{aligned} \tag{3}$$

where Ω_d is the speed of the rotating aerodynamic damping relative to the disk, $\mathscr{C}_f[\cdot]$ models the linearized fluid damping and is a linear spatial operator that is assumed to be self-adjoint and positive-definite with respect to the clamped–free disk boundary conditions. This damping operator includes the dissipative effects of both fluid viscosity and acoustic radiation. Eq. (3) shows that $F(r,\theta,t)$ can also be expressed as a linear combination of a ground-fixed dissipation term and a co-rotating dissipation term. Recently, Jana and Raman (2004) have shown that a three-dimensional inviscid compressible flow model of the fluid surrounding the disk introduces a ground-fixed damping and a small added mass effect into the problem. Because the added mass effect is small for disks in air, it is assumed negligible in this work. It is reasonable to assume that inclusion of fluid viscosity will add to both ground-fixed and co-rotating components of the aerodynamic damping. Thus the form of the overall linearized fluid damping term in Eq. (3) is indeed justified.

From the experimental results, it is apparent that a RTW of a specific nodal diameter number dominates the post-flutter response. Accordingly, it is assumed that over a small range of rotation speeds around the onset of flutter, $w(r,\theta,t)$ can be approximated as

$$w(r,\theta,t) \approx W_{mn}(r)(\mu(t)\cos(n\theta) + \eta(t)\sin(n\theta)), \tag{4}$$

where m and n are the nodal circle and diameter numbers of the RTW that destabilizes at the flutter speed, and $W_{mn}(r)$ is the mass-normalized radial eigenfunction for this RTW. A Galerkin projection of the governing PDEs (Eq. (2)), onto the above pair of (m,n) sine and cosine modes results in the following discretized equations:

$$\ddot{\mu} + 2n\Omega\dot{\eta} + (\omega_{mn}^2 - n^2\Omega^2)\mu + C_r(\dot{\mu} + n\Omega\eta) + C_g\dot{\mu} + \alpha\mu(\mu^2+\eta^2) = 0,$$
$$\ddot{\eta} - 2n\Omega\dot{\mu} + (\omega_{mn}^2 - n^2\Omega^2)\eta + C_r(\dot{\eta} - n\Omega\mu) + C_g\dot{\eta} + \alpha\eta(\mu^2+\eta^2) = 0, \tag{5}$$

where C_r is a coefficient of co-rotating linear damping arising from both disk material damping and fluid damping effects, C_g is a coefficient of ground-fixed damping arising from fluid damping alone and α is the coefficient of structural nonlinearity. Expressions for C_r, C_g and α have been included in the Appendix. The above pair of equations form an autonomous nonlinear gyroscopic system. Note that in general, $C_r = C_r(\Omega)$ and $C_g = C_g(\Omega)$ (Hansen et al., 2001). However, in the following analysis, it is assumed that C_r and C_g remain practically constant for a small range of rotation speeds about the flutter speed.

3.2. Analysis of the discretized equations

The discretized equations for the linear undamped in vacuo rotating disk is obtained by setting $C_d = C_g = 0$ and $\alpha = 0$ in Eqs. (5). The corresponding eigenvalue problem yields the frequencies and radial eigenfunctions of the undamped, in vacuo, rotating disk. It is well-known that the relationship between the rotation speed Ω and the (m, n) co-rotating frequency $\omega_{mn}(\Omega)$ of the undamped in vacuo disk is approximately quadratic (Hansen et al., 2001):

$$\omega_{mn}^2 = \omega_{mn,st}^2 + s_{mn}\Omega^2, \tag{6}$$

where $\omega_{mn,st}$ is the stationary disk frequency and s_{mn} is a constant for the particular disk. $\omega_{mn}(\Omega)$ is extracted from the experiments described in Section 2.2. In addition, $\omega_{mn,st}$ is determined by performing an impact test on the stationary disk. The parameter s_{mn} is then estimated by performing a least square fit of Eq. (6) to the experimental frequency–speed data in the pre-flutter region:

$$s_{mn} = \frac{\sum_i \left(\omega_{mn,i}^2 - \omega_{mn,st}^2\right)\Omega_i^2}{\sum_i \Omega_i^4}. \tag{7}$$

Note that the (m, n) FTW and BTW frequencies of the undamped, in vacuo disk are given by $\omega_{mn} \pm n\omega$. The eigenvalues of the damped linear system (only $\alpha = 0$ in Eqs. (5)) are given by (Hansen et al., 2001)

$$\begin{aligned}
\lambda_{mnf} &\approx \frac{C_r + C_g}{2}\left(1 + \frac{n\Omega C_g}{(C_r + C_g)\omega_{mn}}\right) \pm \mathrm{i}(\omega_{mn} + n\Omega),\\
\lambda_{mnb} &\approx \frac{C_r + C_g}{2}\left(1 - \frac{n\Omega C_g}{(C_r + C_g)\omega_{mn}}\right) \pm \mathrm{i}(\omega_{mn} - n\Omega).
\end{aligned} \tag{8}$$

Flutter occurs when the real part of the RTW eigenvalue vanishes, that is, $\mathrm{Real}(\lambda_{mnb}(\Omega_f)) = 0$. Thus knowing the co-rotating damping coefficient C_r and the flutter speed Ω_f from experiments, the ground-fixed damping coefficient C_g at the flutter speed can be estimated by

$$C_g \approx C_r\left(\frac{n}{\sqrt{\frac{\omega_{mn,st}^2}{\Omega_f^2} + s_{mn}}} - 1\right)^{-1}. \tag{9}$$

The computations are performed for the steel disk whose properties are listed in Table 1. For this steel disk, computations yield $\alpha = 0.0027271$ and $s_{mn} = 6.523$. The experiments show the flutter speed for this disk to be approximately 4425 r.p.m., or $\Omega_f \approx 10.549$, and the flutter mode to be the (0, 3) RTW, that is, $n = 3$. Assuming a typical value of $C_r \approx 0.01$ for steel disks, Eq. (9) then yields $C_g \approx 0.10817$.

Using the above estimated parameter values, a bifurcation analysis of the Eqs. (5) is performed over a small range of rotation speeds about the flutter speed of 4425 r.p.m., using the continuation and bifurcation software AUTO 97 (Doedel et al., 1998). Fig. 8 shows the variations of the computed (0, 3) RTW frequency and amplitude with rotation speed near the flutter speed, and compares them with the experimental values. A Hopf bifurcation of the zero equilibrium solution is detected at the flutter speed. Thus, the primary instability is a Hopf bifurcation. As expected, the location of this Hopf bifurcation is found to be independent of the nonlinear coefficient α.

The branch of periodic solutions emanating from the Hopf bifurcation point is computed in AUTO97. The growth of amplitude of the branch of periodic solutions is strongly influenced by the structural nonlinearity. The greater the value of α, the more suppressed is the amplitude growth. For the value of α calculated using the properties of the steel disk listed in Table 1, the computed amplitudes of the branch of periodic solutions match reasonably well with the

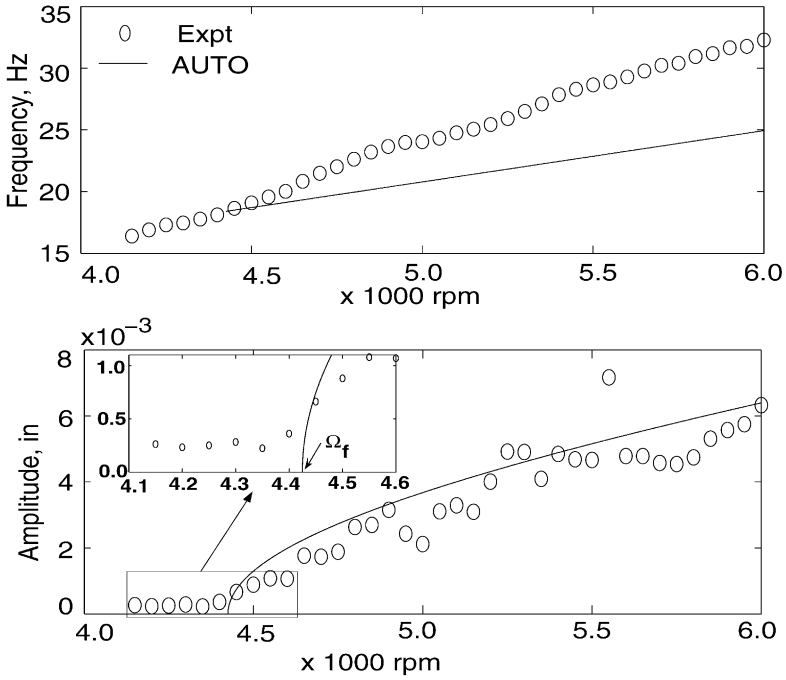

Fig. 8. Comparison of experiment with AUTO computations.

experimentally observed amplitudes near the onset of flutter (Fig. 8(b)). The frequencies of the periodic solutions are slightly underpredicted by the AUTO computations. The difference between the experimental and computed frequencies remains less than 8 Hz over the rotation speed range of 4000–6000 r.p.m. To summarize, a reasonably good quantitative prediction of the primary instability branch is provided by the current nonlinear model.

However, the current model is unable to predict the secondary instabilities and the frequency lock-in phenomena. A complete understanding of the post-flutter response is expected to require advanced nonlinear aerodynamic modeling. Some possibilities in this direction have been discussed in Hansen (1999). The effect of nonlinear interactions between structural modes may also be important at high rotation speeds. Finally, based on the Reynolds numbers presented in Kobayashi et al. (1980), at the flutter speed of 4425 r.p.m., the laminar boundary layer is unstable beyond a radius of approximately 53.34 mm. At 6000 r.p.m., the laminar boundary layer is unstable beyond a radius of approximately 45.72 mm, and the boundary layer is turbulent beyond a radius of approximately 87.38 mm. These numbers suggest that instabilities and turbulence in the boundary layer of the rotating disk may also affect the post-flutter behavior.

4. Conclusions

An experimental and theoretical study of the post-flutter response of a rotating disk is presented. The experiments were performed on a steel as well as a paper disk over a large range of rotation speeds in the post-flutter region, with fine increments of the rotation speed. The current experimental observations are substantially more complicated than those previously reported. Multiple solution branches and secondary bifurcations exist for the unstable travelling wave in the post-flutter region, and transitions between branches are accompanied by jumps in amplitude and frequency. Harmonic distortion of the shape of the unstable wave occur at high post-flutter rotation speeds. Furthermore, small pockets of strong frequency lock-in of the unstable wave may exist, along with an overall approximate frequency lock-in at high rotation speeds in the post-flutter region.

A nonlinear analysis of the disk dynamics over a small range of rotation speeds around the onset of flutter is also presented. The disk is modeled as a centrifugally tensioned von Kármán plate. The aerodynamic load on the disk is represented as a rotating damping pressure, its coefficient assigned a magnitude such that the linear flutter speed matches the experimentally observed value. A Galerkin projection of the governing PDEs is performed onto a single

pair of 1:1 internally resonant sine and cosine modes associated with the unstable RTW. The following key observations are made from an analysis of these discretized equations:

(i) a Hopf bifurcation in the discretized system occurs at the flutter speed;
(ii) the primary instability branch arising out of this Hopf bifurcation is quantitatively predicted reasonably well over a small range of post-flutter rotation speeds;
(ii) the secondary bifurcations and the frequency lock-in phenomena are not predicted by the current model.

Acknowledgements

The authors would like to thank the National Science Foundation (CAREER grant, Award No. 0134455-CMS) and the Purdue Research Foundation for financial support of this research.

Appendix A. Expressions for C_r, C_g and α

The linear damping coefficients C_r and C_g in Eq. (5) are given by the following expressions:

$$C_r = 2\pi \int_a^1 \left(C_d[W_{mn}] + \left(1 - \frac{\Omega_d}{\Omega}\right) C_f[W_{mn}] \right) W_{mn} r \, \mathrm{d}r, \tag{A.1}$$

$$C_g = 2\pi \frac{\Omega_d}{\Omega} \int_a^1 C_f[W_{mn}] W_{mn} r \, \mathrm{d}r. \tag{A.2}$$

Next, it can be shown that for the form of $w(r, \theta, t)$ given by Eq. (4), the membrane stress function caused by nonlinear bending takes the form

$$\Phi_0(r, \theta, t) = \Psi_1(r)\left(\frac{\mu^2 + \eta^2}{2}\right) + \Psi_2(r)\left[\left(\frac{\eta^2 - \mu^2}{2}\right)\cos 2n\theta - \mu\eta \sin 2n\theta\right], \tag{A.3}$$

where $\Psi_1(r)$ and $\Psi_2(r)$ are governed by two boundary value problems in the radial coordinate (Nayfeh, 2000). Then the nonlinear structural stiffness coefficient α is given by

$$\begin{aligned} \alpha_{mn} = & -\pi\varepsilon \int_a^1 \left(\frac{W_{mn,rr}\Psi_{1,r} + W_{mn,r}\Psi_{1,rr}}{2} - \frac{n^2 W_{mn}\Psi_{1,rr}}{2r} \right. \\ & - \frac{W_{mn,rr}\Psi_{2,r} + W_{mn,r}\Psi_{2,rr}}{4} + \frac{(4W_{mn,rr}\Psi_2 + W_{mn}\Psi_{2,rr} + 4W_{mn,r}\Psi_{2,r})n^2}{4r} \\ & \left. - \frac{(W_{mn,r}\Psi_2 + W_{mn}\Psi_{2,r})n^2}{r^2} + \frac{n^2 W_{mn}\Psi_2}{r^3} \right) W_{mn} \, \mathrm{d}r. \end{aligned} \tag{A.4}$$

References

Ahn, T.K., Mote Jr., C.D., 1998. Mode identification of a rotating disk. Experimental Mechanics 38, 250–254.

Bouchard, G., Talke, F.E., 1986. Non-repeatable flutter of magnetic recording disks. IEEE Transactions on Magnetics 22, 1019–1021.

D'Angelo III, C., Mote Jr., C.D., 1993. Aerodynamically excited vibration and flutter of a thin disk rotating at supercritical speed. Journal of Sound and Vibration 168, 15–30.

Doedel, E.J., Champneys, A.R., Fairgrieve, T.F., Kuznetsov, Y.A., Sandstede, B., Wang, X., 1998. Auto 97: Continuation and Bifurcation Software for Ordinary Differential Equations (With HomCont). Concordia University, Montreal, Canada.

Hansen, M.H., 1999. Aeroelasticity and dynamics of spinning disks. DCAMM Report no. S85. Technical University of Denmark, Department of Solid Mechanics, Lyngby, Denmark.

Hansen, M.H., Raman, A., Mote Jr., C.D., 2001. Estimation of nonconservative aerodynamic pressure leading to flutter of spinning disks. Journal of Fluids and Structures 15, 39–57.

Hosaka, H., Crandall, S.H., 1992. Self-excited vibrations of a flexible disk rotating on an air film above a flat surface. Acta Mechanica 3 (Suppl), 115–127.

Huang, F., Mote Jr., C.D., 1995. On the instability mechanisms of a disk rotating close to a rigid surface. Journal of Applied Mechanics 62, 764–771.

Jana, A., Raman, A., 2004. Aeroelastic flutter of a disk rotating in an unbounded acoustic medium. Journal of Sound and Vibration, in press.

Kim, H.R., Renshaw, A.A., 2002. Aeroelastic flutter of circular disks: a simple predictive model. Journal of Sound and Vibration 256, 227–248.

Kim, B.C., Raman, A., Mote Jr., C.D., 2000. Prediction of aeroelastic flutter in a hard disk drive. Journal of Sound and Vibration 238, 309–325.

Kobayashi, R., Kohama, Y., Takamadate, C., 1980. Spiral vortices in boundary layer transition regime on a rotating disk. Acta Mechanica 35, 71–82.

Lee, S.Y., Yoon, D.W., Park, K., 2003. Aerodynamic effect on natural frequency and flutter instability in rotating optical disks. Microsystem Technologies 9, 369–374.

Naganathan, G., Ramadhyani, S., Bajaj, A.K., 2002. Numerical simulations of flutter instability of a flexible disk rotating close to a rigid wall. Journal of Vibration and Control 9, 95–118.

Nayfeh, A.H., 2000. Nonlinear Interactions. Wiley, New York.

Nowinski, J.L., 1964. Nonlinear transverse vibrations of a spinning disk. Journal of Applied Mechanics 31, 72–78.

Nowinski, J.L., 1984. Nonlinear vibrations of an elastic disk rotating in a viscous fluid. Ingenieur-Archiv 54, 291–300.

Raman, A., Hansen, M.H., Mote Jr., C.D., 2002. A note on the post-flutter dynamics of a rotating disk. Journal of Applied Mechanics 69, 864–866.

Renshaw, A.A., 1998. Critical speed for floppy discs. Journal of Applied Mechanics 65, 116–120.

Renshaw, A.A., D'Angelo III, C., Mote Jr., C.D., 1994. Aerodynamically excited vibration of a rotating disc. Journal of Sound and Vibration 177, 577–590.

Stakhiev, Y.M., 1972. Vibrations in thin steel discs. Russian Engineering Journal 52, 14–17.

Yasuda, K., Torii, T., Shimizu, T., 1992. Self-excited oscillations of a circular disk rotating in air. JSME International Journal, Series III 35, 347–352.